Neonatal morphometric similarity mapping for predicting brain age and characterizing neuroanatomic variation associated with preterm birth

Paola Galdi[1,*], Manuel Blesa[1,*], David Q. Stoye[1], Gemma Sullivan[1], Gillian J. Lamb[1], Alan J. Quigley[2], Michael J. Thrippleton[3,4], Mark E. Bastin[3], James P. Boardman[1,3]

[1] *MRC Centre for Reproductive Health, University of Edinburgh, Edinburgh, EH16 4TJ, UK*
[2] *Department of Radiology, Royal Hospital for Sick Children, Edinburgh, EH9 1LF, UK*
[3] *Centre for Clinical Brain Sciences, University of Edinburgh, Edinburgh, EH16 4SB, UK*
[4] *Edinburgh Imaging, University of Edinburgh, Edinburgh, EH16 4SB, UK*
*These authors contributed equally to this work.

Running title: Neonatal morphometric similarity mapping for describing the developing brain

Corresponding Author:
Paola Galdi, PhD
MRC Centre for Reproductive Health, University of Edinburgh, Edinburgh, EH16 4TJ, UK
paola.galdi@ed.ac.uk

Number of pages: 34

Number of figures: 9

Number of extended data figures: 2

Number of tables: 1

Number of extended data tables: 1

Number of words Abstract: 178

Number of words Introduction: 650

Number of words Discussion: 1494

Conflict of Interest: The authors declare no competing financial interests.

Acknowledgements: We are grateful to the families who consented to take part in the study. This work was supported by Theirworld (`www.theirworld.org`) and was undertaken in the MRC Centre for Reproductive Health, which is funded by MRC Centre Grant (MRC G1002033). MJT was supported by NHS Lothian Research and Development Office. Participants were scanned in the University of Edinburgh Imaging Research MRI Facility at the Royal Infirmary of Edinburgh which was established with funding from The Wellcome Trust, Dunhill Medical Trust, Edinburgh and Lothians Research Foundation, Theirworld, The Muir Maxwell Trust and many other sources; we thank the University's imaging research staff for providing the infant scanning.

Abstract

Multi-contrast MRI captures information about brain macro- and micro-structure which can be combined in an integrated model to obtain a detailed "fingerprint" of the anatomical properties of an individual's brain. Inter-regional similarities between features derived from structural and diffusion MRI, including regional volumes, diffusion tensor metrics, neurite orientation dispersion and density imaging measures, can be modelled as morphometric similarity networks (MSNs). Here, individual MSNs were derived from 105 neonates (59 preterm and 46 term) who were scanned between 38 and 45 weeks postmenstrual age (PMA). Inter-regional similarities were used as predictors in a regression model of age at the time of scanning and in a classification model to discriminate between preterm and term infant brains. When tested on unseen data, the regression model predicted PMA at scan with a mean absolute error of 0.70 ± 0.56 weeks, and the classification model achieved 92% accuracy. We conclude that MSNs predict chronological brain age accurately; and they provide a data-driven approach to identify networks that characterize typical maturation and those that contribute most to neuroanatomic variation associated with preterm birth.

Significance Statement

Preterm birth affects 15 million deliveries each year and is closely associated with intellectual disability, educational under-performance and psychiatric disorders. Imaging studies reveal a cerebral signature of preterm birth that includes alterations in brain structure and network connectivity, but there has not been a unified data-driven approach that incorporates all available information from MRI. We report that morphometric similarity networks (MSNs), which integrate information from structural MRI and diffusion MRI in a single model, accurately predict brain age. MSNs reveal the networks that characterize maturation and those that contribute to neuroanatomic variation associated with preterm birth. MSNs are extensible and offer a new approach for investigating early life origins of neurodevelopmental and mental health disorders

Introduction

Preterm birth is closely associated with increased risk of neurodevelopmental, cognitive and psychiatric impairment that extends across the life course (Nosarti et al., 2012; Anderson, 2014; Mathewson et al., 2017; Van Lieshout et al., 2018). Structural and diffusion MRI (sMRI and dMRI) support the conceptualisation of atypical brain growth after preterm birth as a process characterised by micro-structural alteration of connective pathways due to impaired myelination and neuronal dysmaturation (Boardman et al., 2006; Anjari et al., 2007; Counsell et al., 2008; Ball et al., 2013; Back and Miller, 2014; Van Den Heuvel et al., 2015; Eaton-Rosen et al., 2015; Thompson et al., 2016; Batalle et al., 2017; Telford et al., 2017; Batalle et al., 2018); and the ensuing 'dysconnectivity phenotype' could form the basis for long term functional impairment (Boardman et al., 2010; Caldinelli et al., 2017; Keunen et al., 2017; Cao et al., 2017; Batalle et al., 2018b). However, there has not been a unified approach that incorporates all available information from sMRI and dMRI to study brain maturation in the perinatal period so the set of image features that best capture brain maturation, and support image classification, are unknown.

The majority of neonatal connectomics studies have used single modes of data such as dMRI tractography (Brown et al., 2014; Batalle et al., 2017; Blesa et al., 2019) or resting-state functional connectivity (Ball et al., 2016; Smyser et al., 2016a). An alternative connectome model is the structural covariance network (SCN) approach (Alexander-Bloch et al., 2013) in which covariance between regional measurements is calculated across subjects, resulting in a single network for the entire population. Other approaches have constructed subject-specific SCNs (Li et al., 2017; Mahjoub et al., 2018) or higher order morphological networks to model the relationship between ROIs across different views (Soussia and Rekik, 2018), but these techniques have been restricted to the use of morphometric variables available through standard structural T1-weighted MRI sequences and by using a single metric (e.g. cortical thickness) to assess the "connectivity" between nodes (Shi et al., 2012).

Based on observations that integrating data from different MRI sequences enhances anatomic characterization (Melbourne et al., 2014; Kulikova et al., 2015; Ball et al., 2017; Thompson et al., 2018a), we investigated whether whole-brain structural connectomes derived from multi-modal data within a predicting framework capture novel information about perinatal brain development. We used morphometric similarity networks (MSN) to model inter-regional corre-

lations of multiple macro- and micro-structural multi-contrast MRI variables in a single individual. This approach was originally devised to study how human cortical networks underpin individual differences in psychological functions (Seidlitz et al., 2018), and we adapted it to describe both cortical and subcortical regions in the developing brain. The method works by computing for each region of interest (ROI) a number of metrics derived from different MRI sequences which are arranged in a vector. The aim is to obtain a multidimensional description of the structural properties of the ROIs. The MSN is then built considering the ROIs as nodes and modelling connection strength as the correlation between pairs of ROI vectors, thus integrating in a single connectome the ensemble of imaging features. The pattern of inter-regional correlations can be conceptualized as a "fingerprint" of an individual's brain.

We investigated the utility of MSNs for describing brain maturation, and for patient classification. The edges of individual MSNs were used to train two predictive models: a regression model to predict postmenstrual age (PMA) at scan and identify the set of image features that best model chronological brain age; and a classification model to discriminate between preterm and term-born neonates, and thereby identify the networks that explain neuroanatomic variation associated with preterm birth. Compared to simple regression models or correlation analysis, the advantage of predictive models is the possibility to verify that results generalise on unseen data, and hence to assess the validity of MSNs as an integrated representation for studying early brain development brain.

Materials and Methods

Participants and data acquisition

Participants were recruited as part of a longitudinal study designed to investigate the effects of preterm birth on brain structure and long term outcome. The study was conducted according to the principles of the Declaration of Helsinki, and ethical approval was obtained from the UK National Research Ethics Service. Parents provided written informed consent. One hundred and five neonates underwent MRI at term equivalent age at the Edinburgh Imaging Facility: Royal Infirmary of Edinburgh, University of Edinburgh, UK. The study group contained 46 term and 59 preterm infants (details are provided in Table 1). The distribution of PMA at scan for all participants, for the term and preterm groups, and the distribution by gender are shown in Fig. 1. Of the preterm infants, 12 had bronchopulmonary dysplasia, 3 had

71 necrotising enterocolitis and 2 required treatment for retinopathy of prematurity.

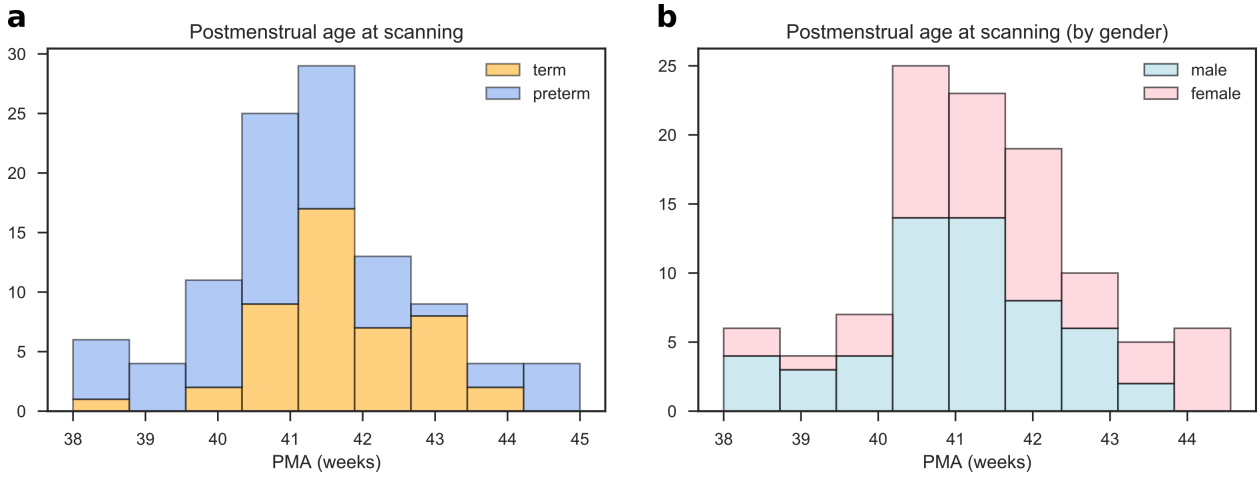

Figure 1. Distribution of postmenstrual age at scan for all subjects. a) Age distribution for the for term (blue) and preterm (orange) groups. b) Age distribution for male (blue) and female (pink) participants.

Table 1. Participant characteristics.

	preterm (N=59)	term (N=46)	all (N=105)
PMA at birth (weeks)	23.42-32.00	37.00-42.00	23.42-42.00
Birth weight (grams)	454-2100	2556-4560	454-4560
PMA at scan (weeks)	38.00-44.56	38.28-43.84	38.00-44.56
M:F ratio	29:30	26:20	55:50

PMA = Postmenstrual age, M = male, F = female.

72 A Siemens MAGNETOM Prisma 3 T MRI clinical scanner (Siemens Healthcare Erlangen, Germany) and 16-channel
73 phased-array paediatric head coil were used to acquire: 3D T1-weighted MPRAGE (T1w) (acquired voxel size = 1mm
74 isotropic) with TI 1100 ms, TE 4.69 ms and TR 1970 ms; 3D T2-weighted SPACE (T2w) (voxel size = 1mm isotropic)
75 with TE 409 ms and TR 3200 ms; and axial dMRI. dMRI was acquired in two separate acquisitions to reduce the time
76 needed to re-acquire any data lost to motion artefact: the first acquisition consisted of 8 baseline volumes (b = 0
77 s/mm^2 [b0]) and 64 volumes with b = 750 s/mm^2, the second consisted of 8 b0, 3 volumes with b = 200 s/mm^2, 6

volumes with b = 500 s/mm^2 and 64 volumes with b = 2500 s/mm^2; an optimal angular coverage for the sampling scheme was applied (Caruyer et al., 2013). In addition, an acquisition of 3 b0 volumes with an inverse phase encoding direction was performed. All dMRI images were acquired using single-shot spin-echo echo planar imaging (EPI) with 2-fold simultaneous multislice and 2-fold in-plane parallel imaging acceleration and 2 mm isotropic voxels; all three diffusion acquisitions had the same parameters (TR/TE 3400/78.0 ms). Images affected by motion artefact were re-acquired multiple times as required; dMRI acquisitions were repeated if signal loss was seen in 3 or more volumes.

Infants were fed and wrapped and allowed to sleep naturally in the scanner. Pulse oximetry, electrocardiography and temperature were monitored. Flexible earplugs and neonatal earmuffs (MiniMuffs, Natus) were used for acoustic protection. All scans were supervised by a doctor or nurse trained in neonatal resuscitation. Structural images were reported by an experienced paediatric radiologist (A.J.Q.) using the system described in Leuchter et al. (2014), and images with evidence of focal parenchymal injury (post-haemorrhagic ventricular dilatation, porencephalic cyst or cystic periventricular leukomalacia), or central nervous system malformation were excluded.

Data preprocessing

All the following preprocessing steps, including maps calculation and quality check, were performed using dcm2niix, FSL, MRtrix, MIRTK, ANTs, Connectome Workbench and cuDIMOT (Smith et al., 2004; Avants et al., 2011; Marcus et al., 2011; Makropoulos et al., 2014; Li et al., 2016; Hernandez-Fernandez et al., 2019; Tournier et al., 2019).

First, all DICOM image files (dMRI and sMRI) were converted to NIFTI (Li et al., 2016). Structural data were preprocessed using the developing Human Connectome Project (dHCP) minimal structural processing pipeline (Makropoulos et al., 2018). Briefly, the T1w image was co-registered to the T2w image, both were corrected for bias field inhomogeinities (Tustison et al., 2010) and an initial brain mask was created (Smith, 2002). Following this, the brain was segmented into different tissue types (CSF: cerebrospinal fluid; WM: white matter; cGM: cortical grey matter; GM: subcortical grey matter) using the Draw-EM algorithm (Makropoulos et al., 2014). Twenty manually labelled atlases (Gousias et al., 2012) were then registered to each subject using a multi-channel registration approach, where the different channels of the registration were the original intensity T2-weighted images and GM probability maps.

These GM probability maps were derived from an initial tissue segmentation, performed using tissue priors propagated through registration of a preterm probabilistic tissue atlas (Serag et al., 2012). The framework produces several output files, but for this study only the aligned T1w and the T2w images and the parcellation in 87 ROIs were used (Makropoulos et al., 2016).

Diffusion MRI processing was performed as follows: for each subject the two dMRI acquisitions were first concatenated and then denoised using a Marchenko-Pastur-PCA-based algorithm (Veraart et al., 2016; Veraart et al., 2016b); the eddy current, head movement and EPI geometric distortions were corrected using outlier replacement and slice-to-volume registration with TOPUP and EDDY (Andersson et al., 2003; Smith et al., 2004; Andersson and Sotiropoulos, 2016; Andersson et al., 2016; Andersson et al., 2017); bias field inhomogeneity correction was performed by calculating the bias field of the mean b0 volume and applying the correction to all the volumes (Tustison et al., 2010). This framework only differs from the optimal pipeline for diffusion preprocessing presented in Maximov et al. (2019) in that we did not perform the final smoothing or the gibbs-ring removal (Kellner et al., 2016) due to the nature of the data (partial fourier space acquisition).

The mean b0 EPI volume of each subject was co-registered to their structural T2w volume using boundary-based registration (Greve and Fischl, 2009), then the inverse transformation was used to propagate ROI labels to dMRI space.

For each ROI, two metrics were computed in structural space: ROI volume and the mean T1w/T2w signal ratio (Glasser and Van Essen, 2011). The other ten metrics were calculated in native diffusion space: five metrics derived from the diffusion kurtosis (DK) model (Jensen et al., 2005) and five derived from the Neurite Orientation Dispersion and Density Imaging model (NODDI) (Zhang et al., 2012; Tariq et al., 2016).

Feature extraction

Structural metrics ROI volumes were calculated without normalising for the whole brain volume; this step is performed later by use of z-score. The mean T1w/T2w signal ratio was calculated before the bias field correction.

The T1w/T2w ratio was used because it enhances myelin contrast and mathematically cancels the signal intensity bias related to the sensitivity profile of radio frequency receiver coils (Glasser and Van Essen, 2011).

Diffusion kurtosis metrics The diffusion kurtosis (DK) model is an expansion of the diffusion tensor model. In addition to the diffusion tensor, the DK model quantifies the degree to which water diffusion in biological tissues is non-Gaussian using the kurtosis tensor. The reason for this is that the Gaussian displacement assumption underlying the diffusion tensor breaks at high b-values (Jensen et al., 2005). We assumed the kurtosis component to be the same along all directions of propagation. The metrics obtained from the DK model for each ROI are the means of: the fractional anisotropy (FA), mean, axial and radial diffusivity (MD, RD, AD) and kurtosis (MK). The MK map quantifies the deviation from Gaussianity of water molecule displacement and can reflect different degrees of tissue heterogeneity (Steven et al., 2014).

NODDI metrics For the NODDI measures, the Bingham distribution was employed (Tariq et al., 2016) in order to extend the NODDI formalism to enable the characterisation of anisotropic orientation dispersion. From this NODDI implementation we obtain five metrics: intracellular volume fraction (υ_{ic}), isotropic volume fraction (υ_{iso}), the orientation dispersion index along the primary and secondary directions (ODI_P and ODI_S) and the overall orientation dispersion index (ODI_{TOT}). NODDI maps were calculated using default parameters.

Data Quality Control

The parcellations obtained after the processing were visually inspected and parcels corresponding to CSF and background parcels were excluded because they do not represent brain tissue. A poor segmentation of the corpus callosum was observed in some of the subjects. Instead of removing the subjects with poor segmentation, we decided to remove the corpus callosum from the model, aiming to maximize the number of subjects. As a result of the whole quality check, we include the whole population and each network is composed of 81 nodes (ROIs).

For the dMRI data we use eddy QC (Bastiani et al., 2019). The quality control is performed at subject level and group

level. Eddy QC provides several measures related to the rotation, translation and outliers of the images. In addition, it also computes the signal-to-noise (SNR) ratio maps of the b0 volumes and the contrast-to-noise (CNR) ratio maps for the different b-values. These maps can be used at group level to visualise the quality of the data (Bastiani et al., 2018). The results show that the overall quality of the data-set was good (Fig. 2). For eddy QC to work, we removed the b-value = 200 s/mm^2. This is because the low number of volumes with this b-value sometimes leads the Gaussian process performed by eddy to produce a perfect fit, which makes the CNR maps unrealistic.

Fig. 2 shows two representative subjects, one from the top quartile of the SNR and CNR distributions (green star) and one from the bottom quartile (red star). In the first panel we can see where they are placed in terms of SNR and CNR over the overall population. The second panel shows the SNR maps (for the b0) and the CNR maps (for the rest of b-values). The bottom panel of the Fig. 2 shows the b0 before and after the processing of the selected subjects. It is possible to observe the effect of the different steps involved, such as the EPI geometric corrections or the bias field inhomogeneity correction.

Experimental design and statistical analysis

The models and the analyses described in this section were implemented in Python (v3.6.4) using open source libraries and frameworks for scientific computing, including SciPy (v1.0.0), Numpy (v1.14.0), Statsmodels (v0.8.0), Pandas (v0.22.0), Scikit-learn (v0.19.1) and Matplotlib (v2.1.2) (Jones et al., 2001; Hunter, 2007; Seabold and Perktold, 2010; McKinney and others, 2010; Pedregosa et al., 2011; Van Der Walt et al., 2011).

Network Construction The MSN for each subject was constructed starting from 81 ROIs; each of the ROI metrics was normalised (z-scored) and Pearson correlations were computed between the vectors of metrics from each pair of ROIs. In this way, the nodes of each network are the ROIs and the edges represent the morphometric similarity between the two related ROIs (Fig. 3). In the following, the terms “edge”, “connection” and “inter-regional similarity” are used interchangeably to refer to the correlation between the regional metrics of a pair of ROIs.

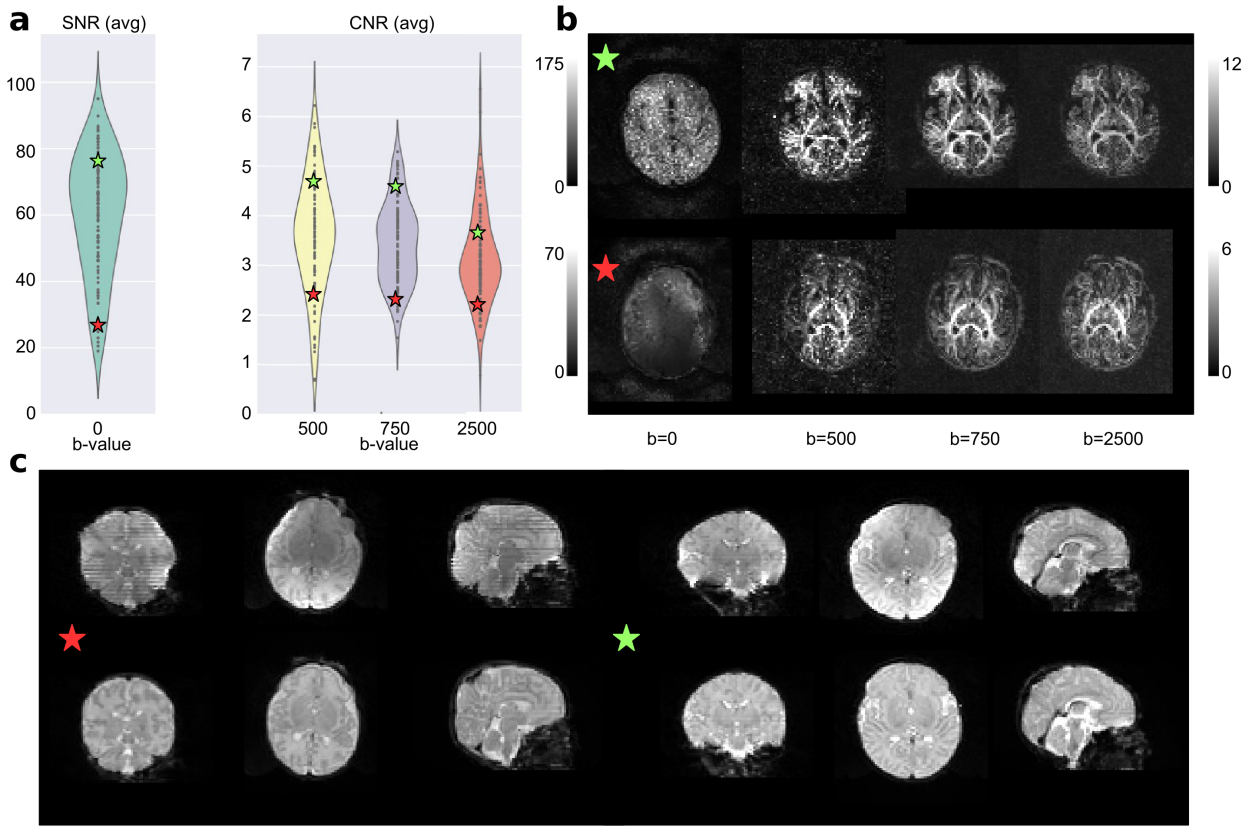

Figure 2. Quality control results. a) Results for the overall population with two selected subjects, one from the top quartile of the SNR and CNR distributions (green star) and the other from the bottom quartile (red star). b) The SNR and CNR maps for the selected subjects. c) The b0 of both subjects before and after the processing pipeline.

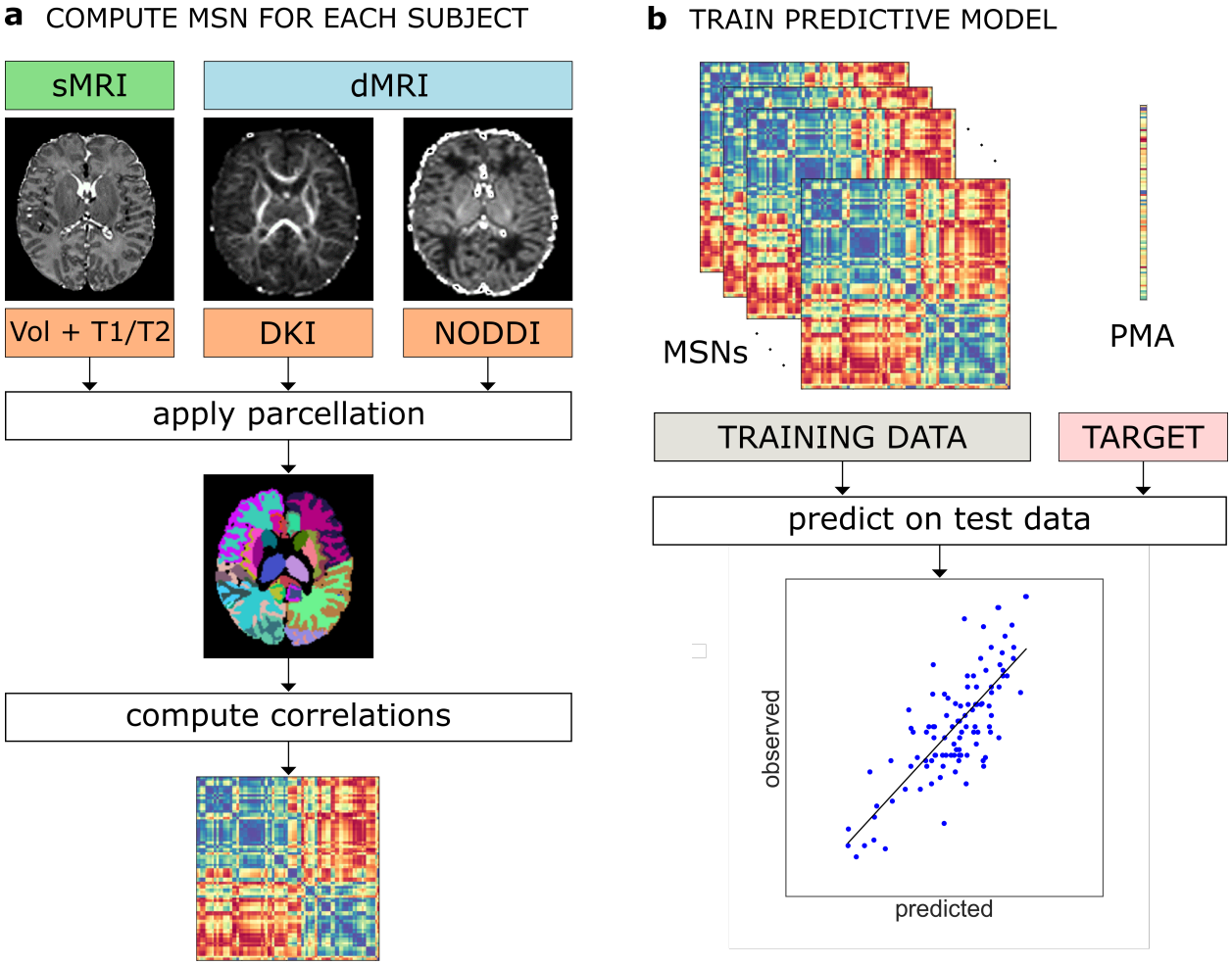

Figure 3. a) Individual MSN construction. Different metrics are extracted from dMRI and sMRI data. The same parcellation is applied to all image types and the average metric values are computed for each ROI. A MSN (represented here as a connectivity matrix) is built by computing the Pearson correlation between the vectors of metrics of each pair of ROIs. b) Training of a predictive model (here for PMA at scan) from individual MSNs. The inter-regional correlations are used as predictor variables in a machine learning model. The performance of the model is evaluated on an independent test set.

Confounding variables We observed a positive correlation ($\rho = 0.27, p = 0.0048$) between PMA at scan and PMA at birth and a negative correlation ($\rho = -0.22, p = 0.0233$) between PMA at scan and gender (coded as a binary variable where 0 indicates female infants and 1 male infants), implying that in our sample term subjects and female subjects tend to have their scan acquired at a later age (see also fig. 1). To control for potential bias, we used these confounders as predictors and compared their predictive performance with our network-based features.

Regression model for age We trained a linear regression model with elastic net regularisation to predict PMA at scan – i.e. chronological brain age – in both preterm and term infants starting from individual MSNs. This model was chosen for its ability to cope with a high number of features (Zou and Hastie, 2005). For each subject, the edges of the MSN (inter-regional correlations) were concatenated to form a feature vector to be given as input to the regression model. Since the connectivity matrix representing the MSN is symmetric, we considered only the upper triangular matrix for each subject. Gender and age at birth were included in the model to control for their possible confounding effects.The prediction performances were evaluated with a leave-one-out cross-validation scheme, by computing the mean absolute error (MAE) averaged across subjects. The parameters of the elastic net were selected with a nested 3-fold cross-validation loop; the folds were stratified in percentiles to include samples covering the whole age range in each of the folds. Permutation testing was used for the statistical validation of the model performance: the null distribution was built by running the age prediction analysis on 1000 random permutation of the PMA.

Classification model A Support Vector Machine (SVM) classifier with linear kernel was trained to discriminate between preterm and term infants. As per the regression model, the input for each subject consisted of inter-regional connections taken from the upper triangular connectivity matrix and age at the time of scanning and gender were included as covariates of no interest.While in the case of regression the elastic net regularisation performs automatically a variable selection step, recursive feature elimination (RFE) was applied in combination with SVM to select the best subset of connections. Model selection was implemented using nested cross validation: an outer 3-fold cross-validation loop was used to select the SVM parameters and an inner 4-fold cross-validation loop was used for RFE. Folds were stratified to include the same proportion of term and preterm subjects. The accuracy of the model was eval-

uated as the number of correctly classified subjects across the leave-one-out folds over the total number of subjects in the test set. The null distribution was built by repeating the exact same analysis 1000 times after randomly assigning subjects to the term and the preterm group.

Feature selection After the preprocessing phase, twelve different metrics were available for each ROI. To study which combination of features produced better performance in the prediction tasks, we implemented a sequential backward-forward feature selection scheme. Starting from the full set of features, at each iteration we removed the feature whose subtraction caused the least increase in prediction error (down to three features, for a total of 73 combinations). The procedure was performed separately for the regression and the classification models.

Results

Feature selection

In figure 4 we report two histograms summarising the performance of the 73 different models compared per each task in the backward feature selection scheme. In both cases, we can observe that the models based on all three data modalities achieved better results in terms of prediction accuracy. The performances of each of the compared model are reported in figure 4-1 and 4-2 for the age prediction and for the classification models, respectively.

The best performing model for age prediction, which was adopted for all subsequent analyses, was based on seven features (Volume, FA, MD, AD, MK, υ_{iso}, ODI_P). Figure 5 shows the average MSN matrix computed across all subjects for the selected set of features and the matrix of correlation between inter-regional similarities and PMA at scan across subjects. The average MSN matrix shows four main blocks that correspond roughly to positive correlations between ROIs within GM and between ROIs within WM, and to negative correlation between WM ROIs and GM ROIs, indicating that ROIs within GM (and within WM) share similar structural properties, while GM and WM regional descriptors tend to be anti-correlated. The four-block structure is recognisable also in the matrix reporting correlations with chronological age: with increasing age regions within GM or within WM become more similar with each other, while the dissimilarities between GM and WM ROIs increases.

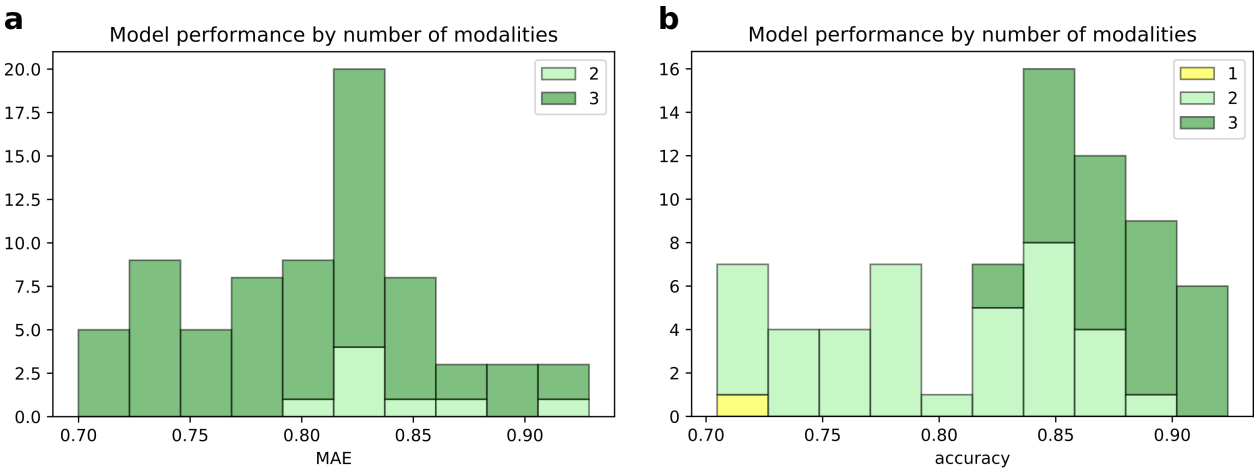

Figure 4. Histograms of the performance of the 73 models compared in the backward feature selection scheme for the age prediction task (a) and for the classification task (b). Bars are grouped by the number of modalities included in the models.

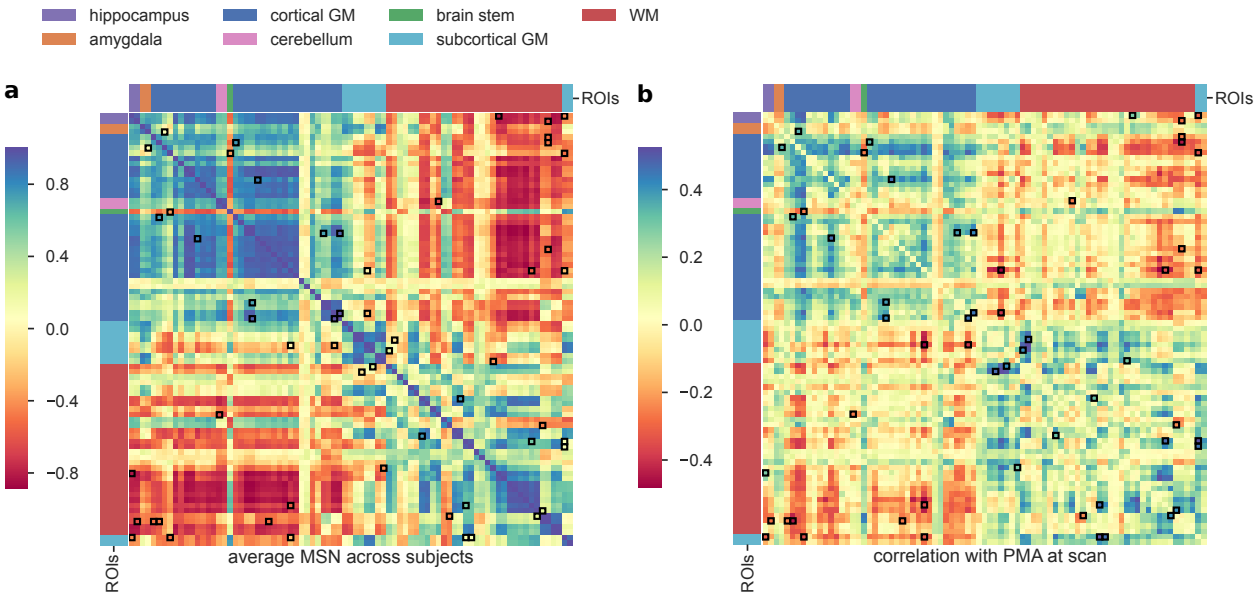

Figure 5. a) Average MSN computed across all subjects using the combination of features selected through the backward feature selection scheme for the age prediction task (Volume, FA, MD, AD, MK, υ_{iso}, ODI_P). b) Correlation between each connection weight (inter-regional similarity) and PMA at scan across subjects. Connections that were identified as predictive features by the predictive model are highlighted in black. ROIs are ordered as in table 5-1.

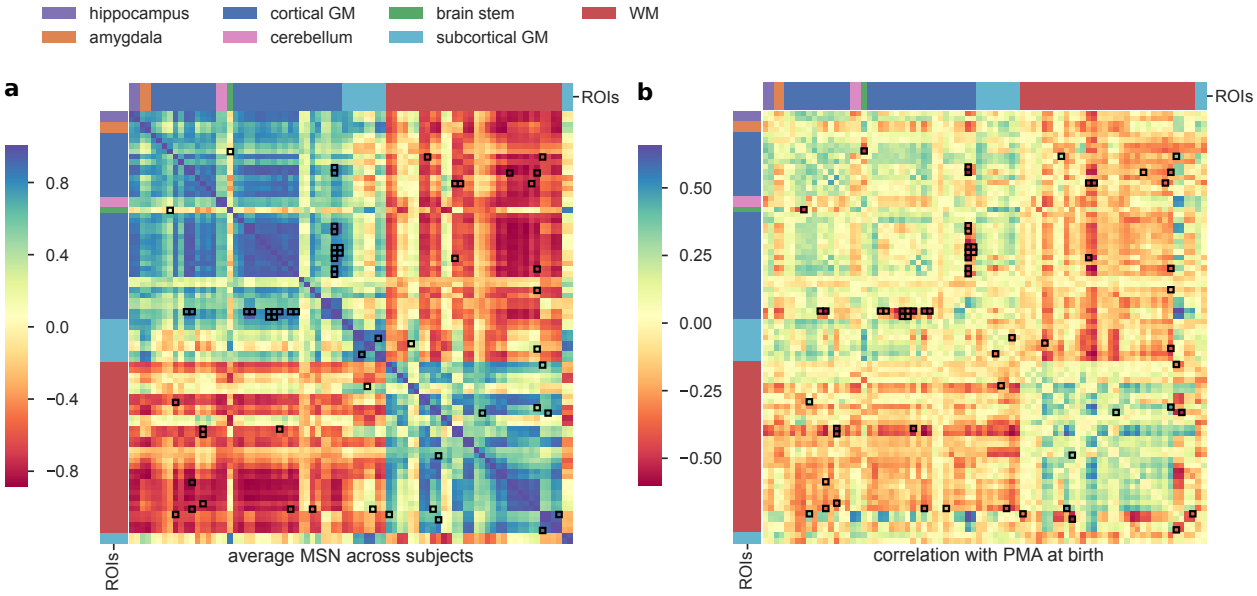

Figure 6. a) Average MSN computed across all subjects using the combination of features selected through the backward feature selection scheme for the classification task (Volume, T1/T2, FA, MD, AD, RD, MK, υ_{ic}, υ_{iso}, ODI_P, ODI_{TOT}). b) Correlation between each connection weight (inter-regional similarity) and PMA at birth across subjects. Connections that were identified as discriminative features by the SVM are highlighted in black. ROIs are ordered as in table 5-1.

The best classifier model was based on eleven out of the twelve features (all except ODI_S), so compared to the age prediction model, four additional features were included: T1/T2, RD, υ_{ic} and ODI_{TOT}. The average MSN computed with the selected features and the matrix of correlation with PMA at birth is shown in figure 6. Comparing panel b of figures 5 and 6, it is apparent that while the patterns of correlation with PMA at scan and at birth are similar within GM and WM, subcortical ROIs show an opposite trend: with increasing PMA at scan subcortical ROIs tend to become more similar to WM ROIs and more dissimilar to GM ROIs, but the similarity between subcortical ROIs and cortical GM is positively correlated to age at birth.

Prediction results

The best regression model predicted chronological age (PMA at scan) with a MAE of 0.70 ± 0.56 weeks on the test data. The results of the permutation test are shown in figure 7. The two confounding variables (gender and age

at birth) were not selected by the internal feature selection procedure, hence the predictions were based on network features alone. For comparison, we evaluated the predictive performance of a linear regression model using only gender and PMA at birth as independent variables, that achieved a MAE of 1.03 ± 0.88 weeks. A Wilcoxon rank-sum test confirmed that the latter model achieved a significantly greater error ($W = 6525, p = 0.0107$).

To study which connections contributed the most to chronological age prediction, we selected only edges which were assigned a non-zero coefficient in at least 99% of cross-validation folds. These edges are shown in the chord diagram in Fig. 8, and are colour coded to distinguish between inter-regional similarities that increase or decrease with age, to highlight networks of regions whose morphological properties are converging (gray) or that tend to differentiate with increasing age (red). Intuitively, these edges connect ROIs whose anatomical and micro-structural properties are changing more than others between 38 and 45 weeks PMA, making the ROIs more or less similar. In other words, it is the relative timing of maturation of different brain tissues to determine the relevance of a connection in the age prediction task. The selected connections are located in both cortical (frontal, temporal, parietal and occipital lobes; insular and posterior cingulate cortex) and subcortical regions (thalamus, subthalamic and lentiform nuclei), in the brain stem and in the cerebellum. These areas have been previously associated with age-related changes and preterm birth (Boardman et al., 2006; Ball et al., 2013; Batalle et al., 2017).

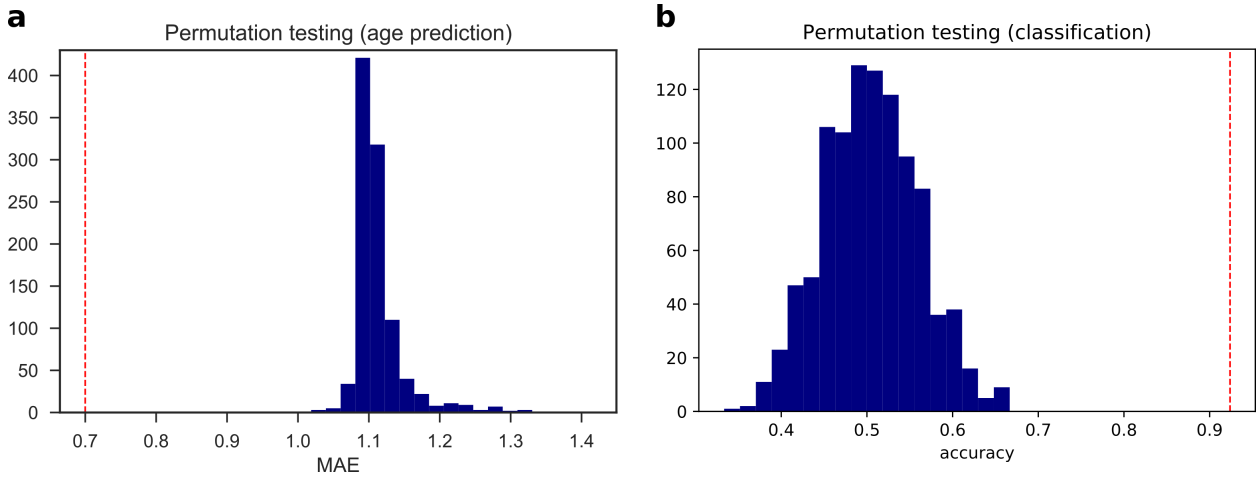

Figure 7. Null distributions computed over 1000 random permutations of the target variable for the age prediction (a) and the classification tasks (b). The red dotted lines indicate the performances of our models.

The best classifier discriminated between term and preterm infants with a 92% accuracy (figure 7). None of the confounders were included among the selected features. A logistic regression model built on the confounders alone did not achieve significant accuracy ($56\%, p = 0.091$).

The network of regions that showed the most divergent pattern of structural brain properties in preterm versus term infants comprised the brain stem, the thalamus and the subthalamic nucleus; WM regions in the frontal and insular lobes; GM regions in the occipital lobe; both WM and GM regions in the temporal and parietal lobes and in the posterior cingulate cortex. The chord diagram of edges selected by 99% of the models is shown in Fig. 9, in red where inter-regional similarities are greater in the term group and in gray where they are greater in the preterm group.

Discussion

These results show that the information encoded in MSNs is predictive of chronological brain age in early life and that MSNs provide a novel data-driven method for investigating neuroanatomic variation associated with preterm birth. MSNs were built by combining features from different imaging sequences that describe complementary aspects of brain structure that have been previously studied in isolation (Makropoulos et al., 2016; Batalle et al., 2017) and the resulting predictive models achieved a high accuracy. Furthermore, the regions identified as most predictive have been previously associated with age-related changes and preterm birth (Boardman et al., 2006; Ball et al., 2013; Batalle et al., 2017; Bouyssi-Kobar et al., 2018). These data suggest that to fully describe morphological variation in the developing brain it may be advantageous to adopt a holistic approach, leveraging the additional information that can be derived from integrating multi-contrast MRI data. The main motivation for using a network-based approach is indeed obtaining a whole-brain description able to capture a developmental pattern. A second reason for working with similarities instead of single regional metrics is methodological: computing edge weights as inter-regional similarities enables an integrated representation of all available metrics in a single network; to work with the original features directly would mean either working with several networks (thus requiring a further step to integrate them) or concatenating all the features in a single predictive model, aggravating the problems related with the "curse of dimensionality".

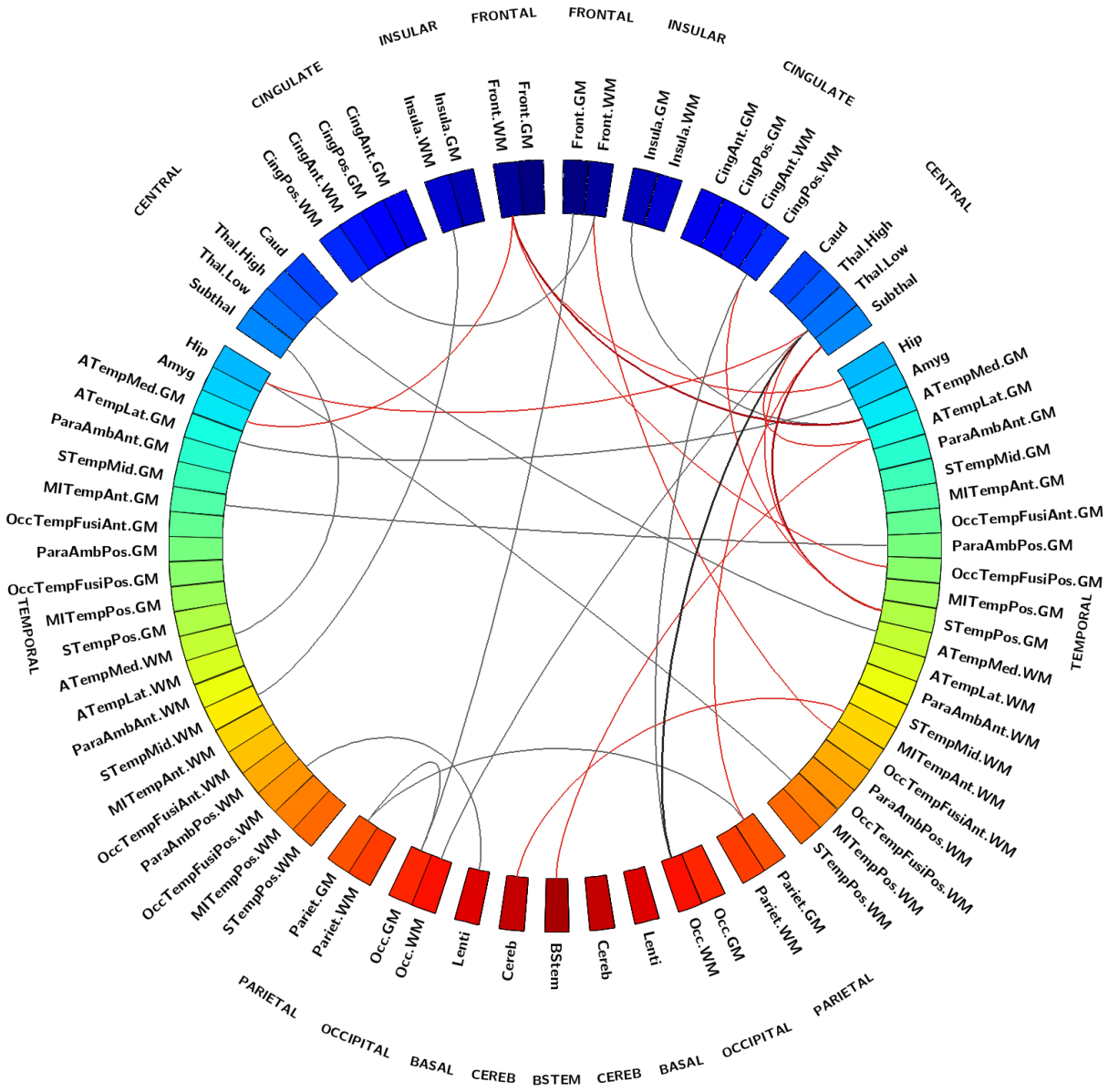

Figure 8. Chord diagram showing MSN edges used for age prediction in at least 99% of regression models in the cross-validation folds. Connections shown in gray are inter-regional similarities that increase with chronological age, while connections in red are inter-regional similarities that decrease with chronological age. The edge width is proportional to the correlation between inter-regional similarities and PMA. The left side of the diagram corresponds to the left side of the brain. Abbreviations for ROI names are explained in table 5-1.

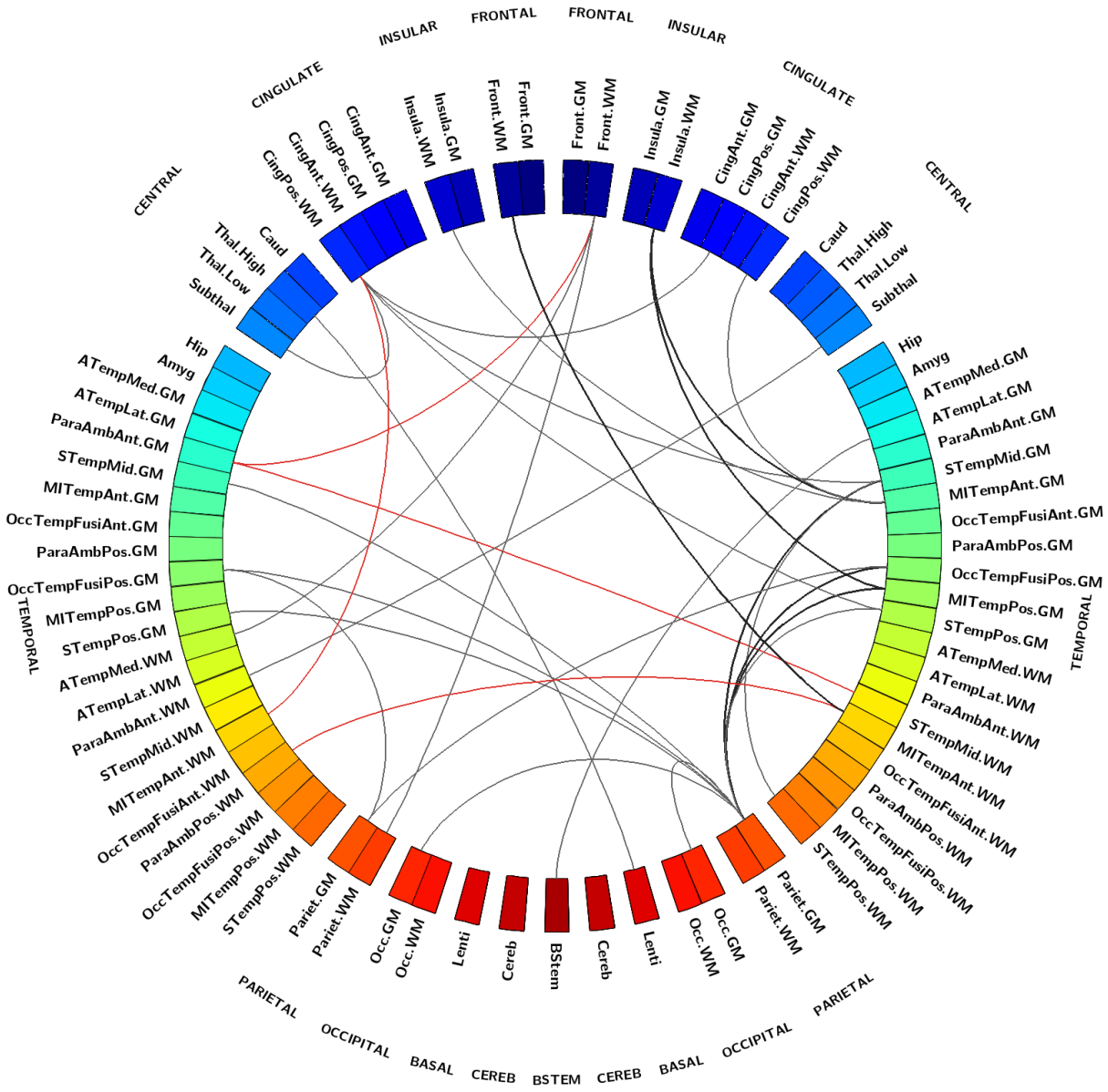

Figure 9. MSN edges showing a divergent pattern of morphological properties in term and preterm infants in at least 99% of classification models in the cross-validation folds. Gray connections indicate inter-regional similarities that are greater in the preterm group, while red connections are greater in the term group. The edge width is proportional to the correlation between inter-regional similarities and prematurity. The left side of the diagram corresponds to the left side of the brain. Abbreviations for ROI names are explained in table 5-1.

Our data are consistent with previous studies of perinatal brain age prediction based on a single type of data or a single metric. For example, Brown et al. (2017) used dMRI tractography to predict brain dysmaturation in preterm infants with brain injury and abnormal developmental outcome and found that altered connectivity in the posterior cingulate gyrus and the inferior orbitofrontal cortex were associated with a delayed maturation; both of these regions are included in the networks identified by our model. Regional FA, MD, MK, and v_{ic} are each predictive of age (Genc et al., 2017; Karmacharya et al., 2018; Ouyang et al., 2019), and the first three measures were selected in our age predicition model. Growth of the thalami and brainstem, defined in terms of myelin-like signals from T2-weighted images, successfully predicted age between 29 and 44 weeks (Deprez et al., 2018) and these regions are included in the networks most predictive of age in the current study. In Toews et al. (2012), scale-invariant image features were extracted from T1-weighted MRI data of 92 subjects over an age range of 8-590 days to build a developmental model that was used to predict age of new subjects; and Ceschin et al. (2018) proposed a deep learning approach to detect subcortical brain dysmaturation from T2-weighted fast spin echo images in infants with congenital hearth disease. Wu et al. (2019) used cortical features extracted from structural images to predict age of 50 healthy subjects with 251 longitudinal MRI scans from 14 to 797 days; compatibly with our results, the regions reported to be important for age prediction were bilateral medial orbitofrontal, parahippocampal, temporal pole, right superior parietal and posterior cingulate cortex. In addition, many works have identified imaging biomarkers associated with preterm birth, such as brain tissue volume (Alexander et al., 2018; Gui et al., 2019), myelin content (Melbourne et al., 2016), and diffusion tensor metrics (Anjari et al., 2007; Bouyssi-Kobar et al., 2018).

The connections most predictive of age revealed that brain maturation is characterised by morphological convergence of some networks and divergence of others (fig. 8). These connections mostly involve fronto-temporal and subcortical ROIs, which suggests that the micro- and macro-structural properties of these regions are highly dynamic between 38-45 weeks. Among these, inter-regional similarities within GM and WM increase with age, similarities between cortical GM and WM decrease, while subcortical ROIs become more similar to WM and more dissimilar to cortical GM. This is consistent with previous findings on the different trends in development of the thalamus and the cortex (Eaton-Rosen et al., 2015). Additionally, in a study of early development of structural networks (Batalle et al., 2017),

connections to and from deep grey matter are reported to show the most rapid developmental changes between 25-45 weeks, while intra-frontal, frontal to cingulate, frontal to caudate and inter-hemispheric connections are reported to mature more slowly.

Conversely, the inter-regional similarities selected by the SVM classifier to discriminate between term and preterm (figures 5 and 9) are more distributed across cortical GM and WM and are for the most part greater in the preterm group. The fact that in the term group these cortical ROIs are less homogeneous in terms of structural properties could be interpreted as a sign that in term infants these regions are at a different stage of maturation where their morphological profile is consolidating along specialized developmental trajectories. It has been previously suggested that the rapid maturation of cortical structures occurring in the perinatal period is vulnerable to the effects of preterm birth (Kostović and Jovanov-Milošević, 2006; Ball et al., 2011; Ball et al., 2013; Smyser et al., 2016b).

The differences between networks identified for age prediction and for preterm classification indicate that atypical brain development after preterm birth is not solely a problem of delayed maturation, but it is characterised by a specific signature. Indeed, while the age prediction networks capture changes occurring in both the preterm and the term group, the classification networks highlights where there are group-wise differences, and they do not match: in the case of a delayed maturation we would have observed differences in the same regions undergoing age-related changes. MSN variations associated with preterm birth affected brain stem, thalami, sub-thalamic nuclei, WM regions in the frontal and insular lobes, GM regions in the occipital lobe, and WM and GM regions in the temporal and parietal lobes and in the posterior cingulate cortex. This distribution of structural variation is consistent with previous reports of regional alteration in brain volume and dMRI parameters based on single contrasts (Boardman et al., 2006; Bonifacio et al., 2010; Ball et al., 2013; Brown et al., 2017; Batalle et al., 2017; Alexander et al., 2018; Thompson et al., 2018b; Bouyssi-Kobar et al., 2018). Furthermore, compared to the age prediction model, the MSNs used for preterm classification are based on four additional metrics: T1/T2, related to myelination; RD, measuring water dispersion; υ_{ic} describing neurite density; and ODI_{TOT}, associated with the fanning of WM tracts. All these metrics contribute to characterise the micro-structural alterations associated with preterm birth (Eaton-Rosen et al., 2015; Melbourne et al., 2016; Batalle et al., 2018; Thompson et al., 2018b; Bouyssi-Kobar et al., 2018).

In both chord diagrams (figures 8 and 9) we observed more edges in the right hemisphere than in the left one, hinting at the existence of a lateralization mechanism in the maturational process. An asymmetry in the development of the right hemisphere in neonates was previously reported in Dubois et al. (2010); Yap et al. (2011); Wu et al. (2019). It is worth noting that both elastic net and SVM models perform a feature selection step to exclude features that are correlated and that carry redundant information in order to improve prediction performance, hence it might be the case that the models selected the right connections and discarded the left ones precisely because they had a similar information content. However, the displayed connections were selected in 99% of the cross-validation folds, therefore if left and right edges were indeed "exchangeable" this disproportion would probably be less stark.

This work has some limitations. First, the decision to include subcortical and white matter structures in the network was made because of prior knowledge of their importance in preterm brain development, but inclusion meant that cortical measures had to be removed from the model, such as sulcal depth or curvature. Second, compared with the original work on MSNs (Seidlitz et al., 2018), we did not have a multi-parametric mapping sequence (Weiskopf et al., 2013); however, because the model is extensible, information from other contrasts could be added and evaluated for their effect on prediction.

Morphology, structural connectivity ad maturation are all influenced by genetics, co-morbidities of preterm birth, and nutrition (Boardman et al., 2014; Anblagan et al., 2016; Sparrow et al., 2016; Krishnan et al., 2016; Ball et al., 2017; Alexander et al., 2018; Blesa et al., 2019). In future work MSNs could offer new understanding of the impact of these factors on integrated measures of brain development, and the relationship between neonatal MSNs and functional outcome could provide novel insights in to the neural bases of cognition and behaviour.

Conclusion

Combining multiple imaging features in a single model enabled a detailed description of the morphological properties of the developing brain that was used inside a predictive framework to identify two networks of regions: the first, predominantly located in subcortical and fronto-temporal areas, that contributed most to age prediction: the second, comprising mostly frontal, parietal, temporal and insular regions, that discriminated between preterm and term born

infant brains. Both predictive models performed best when structural, diffusion tensor-derived and NODDI metrics were combined, which demonstrates the importance of integrating different biomarkers to generate a global picture of the developing human brain.

References

Alexander B, Kelly CE, Adamson C, Beare R, Zannino D, Chen J, Murray AL, Loh WY, Matthews LG, Warfield SK, Anderson PJ, Doyle LW, Seal ML, Spittle AJ, Cheong JL, Thompson DK (2018) Changes in neonatal regional brain volume associated with preterm birth and perinatal factors. *NeuroImage* .

Alexander-Bloch A, Giedd JN, Bullmore E (2013) Imaging structural co-variance between human brain regions. *Nature Reviews Neuroscience* 14:322–336.

Anblagan D, Pataky R, Evans MJ, Telford EJ, Serag A, Sparrow S, Piyasena C, Semple SI, Wilkinson AG, Bastin ME, Boardman JP (2016) Association between preterm brain injury and exposure to chorioamnionitis during fetal life. *Scientific Reports* 6:37932.

Anderson PJ (2014) Neuropsychological outcomes of children born very preterm. *Seminars in Fetal and Neonatal Medicine* 19:90–96.

Andersson JL, Graham MS, Drobnjak I, Zhang H, Filippini N, Bastiani M (2017) Towards a comprehensive framework for movement and distortion correction of diffusion MR images: Within volume movement. *NeuroImage* 152:450–466.

Andersson JL, Graham MS, Zsoldos E, Sotiropoulos SN (2016) Incorporating outlier detection and replacement into a non-parametric framework for movement and distortion correction of diffusion MR images. *NeuroImage* 141:556–572.

Andersson JL, Skare S, Ashburner J (2003) How to correct susceptibility distortions in spin-echo echo-planar images: application to diffusion tensor imaging. *NeuroImage* 20:870 – 888.

Andersson JL, Sotiropoulos SN (2016) An integrated approach to correction for off-resonance effects and subject movement in diffusion MR imaging. *NeuroImage* 125:1063–1078.

Anjari M, Srinivasan L, Allsop JM, Hajnal JV, Rutherford MA, Edwards AD, Counsell SJ (2007) Diffusion tensor imaging with tract-based spatial statistics reveals local white matter abnormalities in preterm infants. *NeuroImage* 35:1021–1027.

Avants BB, Tustison NJ, Song G, Cook PA, Klein A, Gee JC (2011) A reproducible evaluation of ants similarity metric performance in brain image registration. *NeuroImage* 54:2033 – 2044.

Back SA, Miller SP (2014) Brain injury in premature neonates: A primary cerebral dysmaturation disorder? *Annals of Neurology* 75:469–486.

Ball G, Aljabar P, Arichi T, Tusor N, Cox D, Merchant N, Nongena P, Hajnal J, Edwards A, Counsell S (2016) Machine-learning to characterise neonatal functional connectivity in the preterm brain. *NeuroImage* 124:267–275.

Ball G, Aljabar P, Nongena P, Kennea N, Gonzalez-Cinca N et al. (2017) Multimodal image analysis of clinical influences on preterm brain development. *Annals of Neurology* 82:233–246.

Ball G, Boardman JP, Aljabar P, Pandit A, Arichi T, Merchant N, Rueckert D, Edwards AD, Counsell SJ (2013) The influence of preterm birth on the developing thalamocortical connectome. *Cortex* 49:1711 – 1721.

Ball G, Boardman JP, Rueckert D, Aljabar P, Arichi T, Merchant N, Gousias IS, Edwards AD, Counsell SJ (2011) The effect of preterm birth on thalamic and cortical development. *Cerebral Cortex* 22:1016–1024.

Ball G, Srinivasan L, Aljabar P, Counsell SJ, Durighel G, Hajnal JV, Rutherford MA, Edwards AD (2013) Development of cortical microstructure in the preterm human brain. *Proceedings of the National Academy of Sciences* 110:9541–9546.

Bastiani M, Andersson J, Cordero-Grande L, Murgasova M, Hutter J, Price AN, Makropoulos A, Fitzgibbon SP, Hughes E, Rueckert D, Victor S, Rutherford M, Edwards AD, Smith S, Tournier JD, Hajnal JV, Jbabdi S, Sotiropoulos SN (2018) Automated processing pipeline for neonatal diffusion MRI in the developing human connectome project. *NeuroImage* .

Bastiani M, Cottaar M, Fitzgibbon SP, Suri S, Alfaro-Almagro F, Sotiropoulos SN, Jbabdi S, Andersson JL (2019) Automated quality control for within and between studies diffusion MRI data using a non-parametric framework for movement and distortion correction. *NeuroImage* 184:801 – 812.

Batalle D, Edwards AD, O'Muircheartaigh J (2018b) Annual research review: Not just a small adult brain: understanding later neurodevelopment through imaging the neonatal brain. *Journal of Child Psychology and Psychiatry* 59:350–371.

Batalle D, Hughes EJ, Zhang H, Tournier JD, Tusor N, others. (2017) Early development of structural networks and the impact of prematurity on brain connectivity. *NeuroImage* 149:379–392.

Batalle D, O'Muircheartaigh J, Makropoulos A, Kelly CJ, Dimitrova R, Hughes EJ, Hajnal JV, Zhang H, Alexander DC, Edwards AD, Counsell SJ (2018) Different patterns of cortical maturation before and after 38 weeks gestational age demonstrated by diffusion MRI in vivo. *NeuroImage* .

Blesa M, Sullivan G, Anblagan D, Telford EJ, Quigley AJ, Sparrow SA, Serag A, Semple SI, Bastin ME, Boardman JP (2019) Early breast milk exposure modifies brain connectivity in preterm infants. *NeuroImage* 184:431 – 439.

Boardman JP, Counsell SJ, Rueckert D, Kapellou O, Bhatia KK, Aljabar P, Hajnal J, Allsop JM, Rutherford MA, Edwards AD (2006) Abnormal deep grey matter development following preterm birth detected using deformation-based morphometry. *NeuroImage* 32:70–78.

Boardman JP, Walley A, Ball G, Takousis P, Krishnan ML, Hughes-Carre L, Aljabar P, Serag A, King C, Merchant N, Srinivasan L, Froguel P, Hajnal J, Rueckert D, Counsell S, Edwards AD (2014) Common genetic variants and risk of brain injury after preterm birth. *Pediatrics* 133:e1655–e1663.

Boardman J, Craven C, Valappil S, Counsell S, Dyet L, Rueckert D, Aljabar P, Rutherford M, Chew A, Allsop J, Cowan F, Edwards A (2010) A common neonatal image phenotype predicts adverse neurodevelopmental outcome in children born preterm. *NeuroImage* 52:409 – 414.

Bonifacio SL, Glass HC, Chau V, Berman JI, Xu D, Brant R, Barkovich AJ, Poskitt KJ, Miller SP, Ferriero DM (2010) Extreme premature birth is not associated with impaired development of brain microstructure. *The Journal of Pediatrics* 157:726–732.e1.

Bouyssi-Kobar M, Brossard-Racine M, Jacobs M, Murnick J, Chang T, Limperopoulos C (2018) Regional microstructural organization of the cerebral cortex is affected by preterm birth. *NeuroImage: Clinical* 18:871–880.

Brown CJ, Miller SP, Booth BG, Andrews S, Chau V, Poskitt KJ, Hamarneh G (2014) Structural network analysis of brain development in young preterm neonates. *NeuroImage* 101:667 – 680.

Brown CJ, Moriarty KP, Miller SP, Booth BG et al. (2017) Prediction of brain network age and factors of delayed maturation in very preterm infants In *Lecture Notes in Computer Science*, Vol. 10433 LNCS, pp. 84–91.

Caldinelli C, Froudist-Walsh S, Karolis V, Tseng CE, Allin MP, Walshe M, Cuddy M, Murray RM, Nosarti C (2017) White matter alterations to cingulum and fornix following very preterm birth and their relationship with cognitive functions. *NeuroImage* 150:373 – 382.

Cao M, Huang H, He Y (2017) Developmental connectomics from infancy through early childhood. *Trends in neurosciences* 40:494 – 506.

Caruyer E, Lenglet C, Sapiro G, Deriche R (2013) Design of multishell sampling schemes with uniform coverage in diffusion MRI. *Magnetic Resonance in Medicine* 69:1534–1540.

Ceschin R, Zahner A, Reynolds W, Gaesser J, Zuccoli G, Lo CW, Gopalakrishnan V, Panigrahy A (2018) A computational framework for the detection of subcortical brain dysmaturation in neonatal MRI using 3D Convolutional Neural Networks. *NeuroImage* 178:183–197.

Counsell SJ, Edwards AD, Chew ATM, Cowan FM, Boardman JP, Allsop JM, Hajnal JV, Srinivasan L, Dyet LE, Rutherford MA, Anjari M (2008) Specific relations between neurodevelopmental abilities and white matter microstructure in children born preterm. *Brain* 131:3201–3208.

Deprez M, Wang S, Ledig C, Hajnal J, Counsell S, Schnabel J (2018) Segmentation of myelin-like signals on clinical MR images for age estimation in preterm infants. *bioRxiv* .

Dubois J, Benders M, Lazeyras F, Borradori-Tolsa C, Leuchter RHV, Mangin J, Hüppi P (2010) Structural asymmetries of perisylvian regions in the preterm newborn. *NeuroImage* 52:32–42.

Eaton-Rosen Z, Melbourne A, Orasanu E, Cardoso MJ, Modat M, Bainbridge A, Kendall GS, Robertson NJ, Marlow N, Ourselin S (2015) Longitudinal measurement of the developing grey matter in preterm subjects using multi-modal MRI. *NeuroImage* 111:580–589.

Genc S, Malpas CB, Holland SK, Beare R, Silk TJ (2017) Neurite density index is sensitive to age related differences in the developing brain. *NeuroImage* 148:373–380.

Glasser MF, Van Essen DC (2011) Mapping human cortical areas in vivo based on myelin content as revealed by T1- and T2-Weighted MRI. *Journal of Neuroscience* 31:11597–11616.

Gousias IS, Edwards AD, Rutherford MA, Counsell SJ, Hajnal JV, Rueckert D, Hammers A (2012) Magnetic resonance imaging of the newborn brain: Manual segmentation of labelled atlases in term-born and preterm infants. *NeuroImage* 62:1499 – 1509.

Greve DN, Fischl B (2009) Accurate and robust brain image alignment using boundary-based registration. *NeuroImage* 48:63–72.

Gui L, Loukas S, Lazeyras F, Hüppi P, Meskaldji D, Borradori Tolsa C (2019) Longitudinal study of neonatal brain tissue volumes in preterm infants and their ability to predict neurodevelopmental outcome. *NeuroImage* 185:728–741.

Hernandez-Fernandez M, Reguly I, Jbabdi S, Giles M, Smith S, Sotiropoulos SN (2019) Using gpus to accelerate computational diffusion MRI: From microstructure estimation to tractography and connectomes. *NeuroImage* 188:598 – 615.

Hunter JD (2007) Matplotlib: A 2d graphics environment. *Computing in science & engineering* 9:90.

Jensen J, Helpern J, Ramani A, Lu H, Kaczynski K (2005) Diffusional kurtosis imaging: The quantification of non-gaussian water diffusion by means of magnetic resonance imaging. *Magnetic Resonance in Medicine* 53:1432–1440.

Jones E, Oliphant T, Peterson P et al. (2001) SciPy: Open source scientific tools for Python, `http://www.scipy.org/`.

Karmacharya S, Gagoski B, Ning L, Vyas R, Cheng HH, Soul J, Newberger JW, Shenton ME, Rathi Y, Grant PE (2018) Advanced diffusion imaging for assessing normal white matter development in neonates and characterizing aberrant development in congenital heart disease. *NeuroImage: Clinical* 19:360–373.

Kellner E, Dhital B, Kiselev VG, Reisert M (2016) Gibbs-ringing artifact removal based on local subvoxel-shifts. *Magnetic Resonance in Medicine* 76:1574–1581.

Keunen K, Benders MJ, Leemans A, Fieret-Van Stam PC, Scholtens LH, Viergever MA, Kahn RS, Groenendaal F, de Vries LS, van den Heuvel MP (2017) White matter maturation in the neonatal brain is predictive of school age cognitive capacities in children born very preterm. *Developmental Medicine & Child Neurology* 59:939–946.

Kostović I, Jovanov-Milošević N (2006) The development of cerebral connections during the first 20–45 weeks' gestation. *Seminars in Fetal and Neonatal Medicine* 11:415–422.

Krishnan ML, Wang Z, Silver M, Boardman JP, Ball G, Counsell SJ, Walley AJ, Montana G, Edwards AD (2016) Possible relationship between common genetic variation and white matter development in a pilot study of preterm infants. *Brain and behavior* 6:e00434.

Kulikova S, Hertz-Pannier L, Dehaene-Lambertz G, Buzmakov A, Poupon C, Dubois J (2015) Multi-parametric evaluation of the white matter maturation. *Brain Structure and Function* 220:3657–3672.

Leuchter RHV, Gui L, Poncet A, Hagmann C, Lodygensky GA, Martin E, Koller B, Darqué A, Bucher HU, Hüppi PS (2014) Association Between Early Administration of High-Dose Erythropoietin in Preterm Infants and Brain MRI Abnormality at Term-Equivalent Age. *JAMA* 312:817–824.

Li W, Yang C, Shi F, Wu S, Wang Q, Nie Y, Zhang X (2017) Construction of individual morphological brain networks with multiple morphometric features. *Frontiers in Neuroanatomy* 11.

Li X, Morgan PS, Ashburner J, Smith J, Rorden C (2016) The first step for neuroimaging data analysis: Dicom to nifti conversion. *Journal of Neuroscience Methods* 264:47 – 56.

Mahjoub I, Mahjoub MA, Rekik I (2018) Brain multiplexes reveal morphological connectional biomarkers fingerprinting late brain dementia states. *Scientific Reports* 8:4103.

Makropoulos A, Gousias IS, Ledig C, Aljabar P, Serag A, Hajnal JV, Edwards AD, Counsell SJ, Rueckert D (2014) Automatic whole brain MRI segmentation of the developing neonatal brain. *IEEE Transactions on Medical Imaging* 33:1818–1831.

Makropoulos A, Aljabar P, Wright R, Hüning B, Merchant N et al. (2016) Regional growth and atlasing of the developing human brain. *NeuroImage* 125:456–478.

Makropoulos A, Robinson EC, Schuh A, Wright R, Fitzgibbon S et al. (2018) The developing human connectome project: A minimal processing pipeline for neonatal cortical surface reconstruction. *NeuroImage* 173:88–112.

Marcus D, Harwell J, Olsen T, Hodge M, Glasser M, Prior F, Jenkinson M, Laumann T, Curtiss S, Van Essen D (2011) Informatics and data mining tools and strategies for the human connectome project. *Frontiers in Neuroinformatics* 5:4.

Mathewson K, Chow C, Dobson K, Pope E, Schmidt L, Van Lieshout R (2017) Mental health of extremely low birth weight survivors: A systematic review and meta-analysis. *Psychological Bulletin* 143:347 – 383.

Maximov II, Alnaes D, Westlye LT (2019) Towards an optimised processing pipeline for diffusion MRI data: Effects of artefact corrections on diffusion metrics and their age associations in UK Biobank. *bioRxiv* .

McKinney W et al. (2010) Data structures for statistical computing in python In *Proceedings of the 9th Python in Science Conference*, Vol. 445, pp. 51–56. Austin, TX.

Melbourne A, Eaton-Rosen Z, Orasanu E, Price D, Bainbridge A, Cardoso MJ, Kendall GS, Robertson NJ, Marlow N, Ourselin S (2016) Longitudinal development in the preterm thalamus and posterior white matter: MRI correlations between diffusion weighted imaging and T2 relaxometry. *Human Brain Mapping* 37:2479–2492.

Melbourne A, Kendall GS, Cardoso MJ, Gunny R, Robertson NJ, Marlow N, Ourselin S (2014) Preterm birth affects the developmental synergy between cortical folding and cortical connectivity observed on multimodal MRI. *NeuroImage* 89:23–34.

Nosarti C, Reichenberg A, Murray RM, Cnattingius S, Lambe MP, Yin L, MacCabe J, Rifkin L, Hultman CM (2012) Preterm Birth and Psychiatric Disorders in Young Adult Life. *Archives of General Psychiatry* 69:610–617.

Ouyang M, Jeon T, Sotiras A, Peng Q, Mishra V, Halovanic C, Chen M, Chalak L, Rollins N, Roberts TPL, Davatzikos C, Huang H (2019) Differential cortical microstructural maturation in the preterm human brain with diffusion kurtosis and tensor imaging. *Proceedings of the National Academy of Sciences* p. 201812156.

Pedregosa F, Varoquaux G, Gramfort A, Michel V, Thirion B, Grisel O, Blondel M, Prettenhofer P, Weiss R, Dubourg V et al. (2011) Scikit-learn: Machine learning in python. *Journal of machine learning research* 12:2825–2830.

Seabold S, Perktold J (2010) Statsmodels: Econometric and statistical modeling with python In *Proceedings of the 9th Python in Science Conference*, Vol. 57, p. 61. Scipy.

Seidlitz J, Váša F, Shinn M, Romero-Garcia R, Whitaker KJ et al. (2018) Morphometric similarity networks detect microscale cortical organization and predict inter-individual cognitive variation. *Neuron* 97:231–247.e7.

Serag A, Aljabar P, Ball G, Counsell SJ, Boardman JP, Rutherford MA, Edwards AD, Hajnal JV, Rueckert D (2012) Construction of a consistent high-definition spatio-temporal atlas of the developing brain using adaptive kernel regression. *NeuroImage* 59:2255 – 2265.

Shi F, Yap PT, Gao W, Lin W, Gilmore JH, Shen D (2012) Altered structural connectivity in neonates at genetic risk for schizophrenia: A combined study using morphological and white matter networks. *NeuroImage* 62:1622–1633.

Smith SM (2002) Fast robust automated brain extraction. *Human Brain Mapping* 17:143–155.

Smith SM, Jenkinson M, Woolrich MW, Beckmann CF, Behrens TE, Johansen-Berg H, Bannister PR, Luca MD, Drobnjak I, Flitney DE, Niazy RK, Saunders J, Vickers J, Zhang Y, Stefano ND, Brady JM, Matthews PM (2004) Advances in functional and structural mr image analysis and implementation as fsl. *NeuroImage* 23:S208 – S219 Mathematics in Brain Imaging.

Smyser CD, Dosenbach NU, Smyser TA, Snyder AZ, Rogers CE, Inder TE, Schlaggar BL, Neil JJ (2016a) Prediction of brain maturity in infants using machine-learning algorithms. *NeuroImage* 136:1–9.

525 Smyser TA, Smyser CD, Rogers CE, Gillespie SK, Inder TE, Neil JJ (2016b) Cortical gray and adjacent white matter
526 demonstrate synchronous maturation in very preterm infants. *Cerebral Cortex* 26:3370–3378.

527 Soussia M, Rekik I (2018) Unsupervised manifold learning using high-order morphological brain networks derived
528 from T1-w MRI for autism diagnosis. *Frontiers in Neuroinformatics* 12:70.

529 Sparrow S, Manning JR, Cartier J, Anblagan D, Bastin ME, Piyasena C, Pataky R, Moore EJ, Semple SI, Wilkinson
530 AG, Evans M, Drake AJ, Boardman JP (2016) Epigenomic profiling of preterm infants reveals DNA methylation
531 differences at sites associated with neural function. *Translational psychiatry* 6:e716.

532 Steven AJ, Zhuo J, Melhem ER (2014) Diffusion kurtosis imaging: an emerging technique for evaluating the mi-
533 crostructural environment of the brain. *AJR. American journal of roentgenology* 202 1:W26–33.

534 Tariq M, Schneider T, Alexander DC, Wheeler-Kingshott CAG, Zhang H (2016) Bingham-NODDI: Mapping
535 anisotropic orientation dispersion of neurites using diffusion MRI. *NeuroImage* 133:207 – 223.

536 Telford EJ, Cox SR, Fletcher-Watson S, Anblagan D, Sparrow S, Pataky R, Quigley A, Semple SI, Bastin ME,
537 Boardman JP (2017) A latent measure explains substantial variance in white matter microstructure across the new-
538 born human brain. *Brain Structure and Function* 222:4023–4033.

539 Thompson DK, Chen J, Beare R, Adamson CL, Ellis R, Ahmadzai ZM, Kelly CE, Lee KJ, Zalesky A, Yang JY,
540 Hunt RW, Cheong JL, Inder TE, Doyle LW, Seal ML, Anderson PJ (2016) Structural connectivity relates to perinatal
541 factors and functional impairment at 7years in children born very preterm. *NeuroImage* 134:328 – 337.

542 Thompson DK, Kelly CE, Chen J, Beare R, Alexander B, Seal ML, Lee K, Matthews LG, Anderson PJ, Doyle LW,
543 Spittle AJ, Cheong JL (2018a) Early life predictors of brain development at term-equivalent age in infants born
544 across the gestational age spectrum. *NeuroImage* .

545 Thompson DK, Kelly CE, Chen J, Beare R, Alexander B, Seal ML, Lee KJ, Matthews LG, Anderson PJ, Doyle LW,
546 Cheong JL, Spittle AJ (2018b) Characterisation of brain volume and microstructure at term-equivalent age in infants
547 born across the gestational age spectrum. *NeuroImage: Clinical* p. 101630.

548 Toews M, Wells WM, Zöllei L (2012) A feature-based developmental model of the infant brain in structural MRI In
549 *International Conference on Medical Image Computing and Computer-Assisted Intervention*, pp. 204–211. Springer.

550 Tournier JD, Smith RE, Raffelt DA, Tabbara R, Dhollander T, Pietsch M, Christiaens D, Jeurissen B, Yeh CH, Con-
551 nelly A (2019) Mrtrix3: A fast, flexible and open software framework for medical image processing and visualisation.
552 *bioRxiv* .

553 Tustison NJ, Avants BB, Cook PA, Zheng Y, Egan A, Yushkevich PA, Gee JC (2010) N4ITK: Improved N3 bias
554 correction. *IEEE Transactions on Medical Imaging* 29:1310–1320.

555 Van Den Heuvel MP, Kersbergen KJ, De Reus MA, Keunen K et al. (2015) The neonatal connectome during preterm
556 brain development. *Cerebral Cortex* 25:3000–3013.

557 Van Der Walt S, Colbert SC, Varoquaux G (2011) The numpy array: a structure for efficient numerical computation.
558 *Computing in Science & Engineering* 13:22.

559 Van Lieshout RJ, Ferro MA, Schmidt LA, Boyle MH, Saigal S, Morrison KM, Mathewson KJ (2018) Trajectories of
560 psychopathology in extremely low birth weight survivors from early adolescence to adulthood: a 20-year longitudinal
561 study. *Journal of Child Psychology and Psychiatry* 59:1192–1200.

562 Veraart J, Fieremans E, Novikov DS (2016) Diffusion MRI noise mapping using random matrix theory. *Magnetic*
563 *Resonance in Medicine* 76:1582–1593.

564 Veraart J, Novikov DS, Christiaens D, Ades-aron B, Sijbers J, Fieremans E (2016b) Denoising of diffusion MRI
565 using random matrix theory. *NeuroImage* 142:394–406.

566 Weiskopf N, Suckling J, Williams G, Correia MM, Inkster B, Tait R, Ooi C, Bullmore ET, Lutti A (2013) Quantitative
567 multi-parameter mapping of R1, PD*, MT, and R2* at 3T: a multi-center validation. *Frontiers in Neuroscience* 7.

568 Wu Z, Li G, Shen D, Hu D, Lin W (2019) Hierarchical rough-to-fine model for infant age prediction based on cortical
569 features. *IEEE Journal of Biomedical and Health Informatics* pp. 1–1.

570 Yap PT, Fan Y, Chen Y, Gilmore JH, Lin W, Shen D (2011) Development trends of white matter connectivity in the
571 first years of life. *PLoS ONE* 6:e24678.

572 Zhang H, Schneider T, Wheeler-Kingshott CA, Alexander DC (2012) NODDI: Practical in vivo neurite orientation
573 dispersion and density imaging of the human brain. *NeuroImage* 61:1000–1016.

574 Zou H, Hastie T (2005) Regularization and variable selection via the elastic net. *Journal of the Royal Statistical*
575 *Society: Series B (Statistical Methodology)* 67:301–320.

576 Table Legends

577 **Table 1** Participant characteristics.

578

579

580 Figure Legends

581 **Figure 1** Distribution of postmenstrual age at scan for all subjects. a) Age distribution for the for term (blue) and
582 preterm (orange) groups. b) Age distribution for male (blue) and female (pink) participants.

583

584 **Figure 2** Quality control results. a) Results for the overall population with two selected subjects, one from the
585 top quartile of the SNR and CNR distributions (green star) and the other from the bottom quartile (red star). b) The
586 SNR and CNR maps for the selected subjects. c) The b0 of both subjects before and after the processing pipeline.

587

588 **Figure 3** a) Individual MSN construction. Different metrics are extracted from dMRI and sMRI data. The same
589 parcellation is applied to all image types and the average metric values are computed for each ROI. A MSN (repre-
590 sented here as a connectivity matrix) is built by computing the Pearson correlation between the vectors of metrics of
591 each pair of ROIs. b) Training of a predictive model (here for PMA at scan) from individual MSNs. The inter-regional
592 correlations are used as predictor variables in a machine learning model. The performance of the model is evaluated

593 on an independent test set.

594

595 **Figure 4** Histograms of the performance of the 73 models compared in the backward feature selection scheme for the
596 age prediction task (a) and for the classification task (b). Bars are grouped by the number of modalities included in the
597 models.

598

599 **Figure 5** a) Average MSN computed across all subjects using the combination of features selected through the back-
600 ward feature selection scheme for the age prediction task (Volume, FA, MD, AD, MK, υ_{iso}, ODI_P). b) Correlation
601 between each connection weight (inter-regional similarity) and PMA at scan across subjects. Connections that were
602 identified as predictive features by the predictive model are highlighted in black. ROIs are ordered as in table 5-1.

603

604 **Figure 6** a) Average MSN computed across all subjects using the combination of features selected through the back-
605 ward feature selection scheme for the classification task (Volume, T1/T2, FA, MD, AD, RD, MK, υ_{ic}, υ_{iso}, ODI_P,
606 ODI_{TOT}). b) Correlation between each connection weight (inter-regional similarity) and PMA at birth across subjects.
607 Connections that were identified as discriminative features by the SVM are highlighted in black. ROIs are ordered as
608 in table 5-1.

609

610 **Figure 7** Null distributions computed over 1000 random permutations of the target variable for the age prediction
611 (a) and the classification tasks (b). The red dotted lines indicate the performances of our models.

612

613 **Figure 8** Chord diagram showing MSN edges used for age prediction in at least 99% of regression models in the
614 cross-validation folds. Connections shown in gray are inter-regional similarities that increase with chronological age,
615 while connections in red are inter-regional similarities that decrease with chronological age. The edge width is pro-
616 portional to the correlation between inter-regional similarities and PMA. The left side of the diagram corresponds to
617 the left side of the brain. Abbreviations for ROI names are explained in table 5-1.

618

Figure 9 MSN edges showing a divergent pattern of morphological properties in term and preterm infants in at least 99% of classification models in the cross-validation folds. Gray connections indicate inter-regional similarities that are greater in the preterm group, while red connections are greater in the term group. The edge width is proportional to the correlation between inter-regional similarities and prematurity. The left side of the diagram corresponds to the left side of the brain. Abbreviations for ROI names are explained in table 5-1.

Extended Data Legends

Figure 4-1 Feature selection results for the age prediction task. The best set of features was selected with a backward feature selection scheme: starting from the full set of features, at each iteration the feature whose subtraction caused the least increase in prediction error was removed. The mean absolute error (MAE) computed with leave-one-out cross-validation is reported for each subset of features. The black lines depict standard deviation.

Figure 4-2 Feature selection results for the classification task. The best set of features was selected with a backward feature selection scheme: starting from the full set of features, at each iteration the feature whose subtraction caused the least decrease in prediction accuracy was removed. The accuracy computed with leave-one-out cross-validation is reported for each subset of features. The black lines depict standard deviation.

Table 5-1 Abbreviations of ROI names and division of ROIs into groups.